

A *Chandra* Study of the Image Power Spectra of 41 Cool Core and Non-Cool Core Galaxy Clusters

Chenhao Zhang¹, Haiguang Xu^{1,2}, Zhenghao Zhu¹, Weitian Li¹, Dan Hu¹, Jingying Wang⁴,
Junhua Gu⁴, Liyi Gu⁵, Zhongli Zhang⁶, Chengze Liu¹, Jie Zhu³ AND Xiang-Ping Wu⁴

Received _____; accepted _____

¹Department of Physics and Astronomy, Shanghai Jiao Tong University, 800 Dongchuan Road, Minhang, Shanghai 200240, China; email: eotss813@sjtu.edu.cn, hgxu@sjtu.edu.cn;

²IFSA Collaborative Innovation Center, Shanghai Jiao Tong University, 800 Dongchuan Road, Minhang, Shanghai 200240, China

³Department of Electronic Engineering, Shanghai Jiao Tong University, 800 Dongchuan Road, Minhang, Shanghai 200240, China.

⁴National Astronomical Observatories, Chinese Academy of Sciences, 20A Datun Road, Beijing 100012, China;

⁵SRON Netherlands Institute for Space Research, Sorbonnelaan 2, 3584 CA Utrecht, the Netherlands

⁶Max-Planck-Institut für Astrophysik, Karl-Schwarzschild-Straße 1, 85740 Garching, Germany

ABSTRACT

In this work we propose a new diagnostic to segregate cool core (CC) clusters from non-cool core (NCC) clusters by studying the two-dimensional power spectra of the X-ray images observed with the *Chandra* X-ray observatory. Our sample contains 41 members ($z = 0.01 \sim 0.54$), which are selected from the *Chandra* archive when a high photon count, an adequate angular resolution, a relatively complete detector coverage, and coincident CC-NCC classifications derived with three traditional diagnostics are simultaneously guaranteed. We find that in the log-log space the derived image power spectra can be well represented by a constant model component at large wavenumbers, while at small wavenumbers a power excess beyond the constant component appears in all clusters, with a clear tendency that the excess is stronger in CC clusters. By introducing a new CC diagnostic parameter, i.e., the power excess index (PEI), we classify the clusters in our sample and compare the results with those obtained with three traditional CC diagnostics. We find that the results agree with each other very well. By calculating the PEI values of the simulated clusters, we find that the new diagnostic works well at redshifts up to 0.5 for intermediately sized and massive clusters with a typical *Chandra* or *XMM-Newton* pointing observation. The new CC diagnostic has several advantages over its counterparts, e.g., it is free of the effects of the commonly seen centroid shift of the X-ray halo caused by merger event, and the corresponding calculation is straightforward, almost irrelevant to the complicated spectral analysis.

Subject headings: galaxies: clusters: general — galaxies: clusters: intracluster medium — techniques: imaging spectroscopy — X-rays: galaxies: clusters

1. INTRODUCTION

X-ray observations performed in the past two decades have revealed that more than half of the galaxy clusters host a bright, dense core where the intracluster medium (ICM) has cooled down to temperatures lower than that of the ambient gas, so that such cool core (CC; a nomenclature proposed by Molendi & Pizzolato 2001) clusters usually exhibit sharply peaked central X-ray emission. For example, based on the deprojected imaging analysis of an *Einstein* sample of 207 clusters White et al. (1997) found that cool cores appear in $62^{+12}_{-15}\%$ of the clusters. Almost at the same time Peres et al. (1998) studied a *ROSAT* sample of 55 clusters and estimated that 70 – 90% of the sample members can be classified as cool core systems. Later Chen et al. (2007) presented an imaging spectroscopic study of both *ASCA* and *ROSAT* data of 106 clusters, which were drawn from the HIFLUGCS (the Highest X-ray Flux Galaxy Cluster Sample; Reiprich 2001; Reiprich & Böhringer 2002) sample, and concluded that about 49% of the sample clusters have cool cores. Recently by analyzing the *Chandra* data of a statistically complete sample of 64 X-ray selected HIFLUGCS clusters Hudson et al. (2010) found that the chance of the presence of cool core is 72% (the different claimed CC-fractions is mainly as a result of different definitions of CC, e.g., see Hudson et al. (2010) for study of different CC-diagnostics). Despite the fact that all these samples whose redshifts are mostly within 0.2, are flux-limited and thus may be biased to a certain degree toward clusters with a bright core, it is very clear that the cool core can be regarded as a common phenomenon in clusters located at $z \lesssim 0.2$.

The characteristic radiative cooling time of a typical cool core is shorter than the age of the cluster, thus a significant cooling flow of a mass deposition rate of $\sim 10^{2-3} \text{ M}_{\odot} \text{ yr}^{-1}$ should have been operating as predicted by the traditional cooling flow model (e.g., Fabian 1994). However, the observed X-ray gas temperatures of the cool cores never fall below a few keV, and much less cooling signature is found than if cooling-flows progressed unim-

ped in radio, infrared, optical, and UV bands for the gases postulated to have a broad spectrum of temperature, especially those cooled rapidly to $< 10^4$ K. The contradiction between theory and observation invokes additional heating mechanisms (see Makishima et al. 2001, McNamara & Nulsen 2007, and Fabian 2012 for a comprehensive review), among which the heating provided by Active Galactic Nuclei (AGN) is the most prevalent one since it is both adequately energetic and self-regulated. Actually a clear CC-AGN connection has been suggested via the detections of X-ray cavities, jets, lobes, and probably radio mini-halos (radio mini-halos are not unambiguously linked to the AGN, e.g., Feretti et al. 2012) surrounding the radio-loud brightest cluster galaxies (BCGs) on roughly the same scales of the cool cores (e.g., Fabian et al. 2006; Wise et al. 2007; Baldi et al. 2009; Blanton et al. 2011). In about 70% of the CC clusters the central dominating galaxy appears as a radio galaxy (e.g., Burns 1990; Dunn & Fabian 2006; Best et al. 2007; Mittal et al. 2009), and in nearly all CC clusters a radio emitting AGN creating cavities in the X-ray gas is found (e.g., Burns 1990; Eilek 2004; Sanderson et al. 2006; Fabian 2012), notice that the radio-fraction depends on the strength of the CC (i.e. fraction increases from $\sim 67\%$ to $\sim 100\%$ for weak CC clusters to strong CC clusters, Mittal et al. 2009). On the other hand, Sun (2009) found that in a *Chandra* sample containing 152 groups and clusters all 69 BCGs with a 1.4 GHz power exceeding 2×10^{23} W Hz $^{-1}$ possess cool cores. Therefore, it is natural to speculate that the AGN outbursts suppress the overcooling of a CC cluster’s core region and maintain the cluster in the CC state, meanwhile the feedback from the cooling gas in the cool core fuels and regulates the AGN activity (e.g., Donahue et al. 2005).

Although the scenario that AGN and cool core interact with each other in an adaptive way is self-consistent, it does not fully agree with the observations of non-cool core (NCC) clusters, where the cool core has been prevented from forming and the fueling of the AGN is expected to have been quenched. The first counterintuitive case was reported by Gastaldello et al. (2008). The authors found that in the relaxed poor cluster AWM 4 the gas temperature

shows a relatively flat distribution at ~ 2.6 keV and drops outwards quickly at $\gtrsim 200$ kpc, inferring that the cool core has been erased by a a past, major heating episode. This is supported by the facts that the corresponding central cooling time ($\simeq 3$ Gyr) is long and the central gas entropy is high. Even with the newest high-quality *Chandra* data only a tiny cool core-like feature or a galactic corona can be identified within the innermost 2 kpc (Sun 2009; O’Sullivan et al. 2010). In contrast to A1650 and A2244 that show similar thermodynamic properties (Donahue et al. 2005), however, AWM 4 harbors an intermediately active central radio galaxy with extended radio lobes out to 100 kpc, which indicates that NCC system can also possess an AGN. In fact similar AGN outbursts also appear in about 45% of the NCC systems (Mittal et al. 2009; see also Sun 2009 and references therein). Apparently these results expose our poor understanding about the CC-AGN relationship, raising the challenging question as to whether there exists a distinct difference between CC and NCC clusters; in other words, is the dichotomal classification of CC and NCC systems intrinsically reliable? To answer the question a deeper comparison between the X-ray properties of CC and NCC clusters is apparently necessary.

In order to define the CC-NCC dichotomy different diagnostics have been proposed in terms of, e.g., central temperature drop (e.g., Sanderson et al. 2006; Burns et al. 2008), central cooling time (e.g., Bauer et al. 2005; O’Hara et al. 2006; Donahue 2007), surface brightness concentration (e.g., Santos et al. 2008), mass deposition rate (e.g., Chen et al. 2007), or X-ray surface brightness cuspieness (e.g., Vikhlinin et al. 2007). To determine which one of these can be used to unambiguously segregate CC from NCC clusters Hudson et al. (2010) applied 16 CC diagnostics to a sample of 64 HIFLUGCS clusters ($z \lesssim 0.2$), and found that the central cooling time is the best diagnostic parameter for nearby clusters with high quality data, whereas the cuspieness is the best for high redshift ($z \gtrsim 0.03$) clusters. In this work we further address this issue by introducing a new CC diagnostic based on the study of the X-ray image power spectra, which may provide an exquisitely detailed view

of the imaging information (e.g., Walker et al. 2015; Zhuravleva et al. 2015), of 41 galaxy clusters ($z = 0.01 \sim 0.54$) selected from the *Chandra*’s 15-year data archive. The paper is organized as follows. In §2 we describe sample selection criteria and data preparation. In §3, we present data analysis and calculation of image power spectra. In §4 and §5 we discuss our results and summarize the work, respectively. Throughout the paper we adopt a flat Λ CDM cosmology with density parameters $\Omega_m = 0.27$ and $\Omega_\Lambda = 0.73$, and Hubble constant $H_0 = 71 \text{ km s}^{-1} \text{ Mpc}^{-1}$. Unless stated otherwise, we adopt the solar abundance standards in Grevesse & Sauval (1998) and quote errors at 68% confidence level.

2. SAMPLE SELECTION AND DATA PREPARATION

In order to characterize the power spectrum of the X-ray image of a galaxy cluster, a high photon count, an adequate angular resolution, and a relatively complete detector coverage of the cluster should be guaranteed simultaneously. Therefore we constructed our sample by searching the *Chandra* archive for all public pointing observations¹ of galaxy clusters that satisfies the following three criteria: (1) the cluster was observed out to at least $0.45r_{500}$ (r_{500} is defined as the radius within which the mean density of the enclosed gravitating mass is 500 times the critical density of the universe at the cluster’s redshift; see §3.2.3), meanwhile the $\lesssim 0.35r_{500}$ regions is fully or nearly fully covered by the S3 or I0-3 CCDs of the *Chandra* Advanced CCD Imaging Spectrometer (ACIS), (2) the number of the photons collected within $< 0.45r_{500}$ during the observation is more than 12500 cts, and (3) the cluster should have been classified explicitly as a strong cool core (SCC), weak cool core (WCC), or non-cool core (NCC) system coincidentally with three traditional CC diagnostics (i.e., diagnostics based on the calculations of central cooling time, cuspiness, and

¹until October 1st, 2015

concentration parameter; §3.2.4). With these selection criteria we selected 41 galaxy clusters as the sample members, whose basic properties are listed in Table 1.

For each cluster we started from the ACIS level-1 event files and followed the standard *Chandra* data processing procedure to reduce the data with CIAO v4.4 and CALDB v4.4.8. To be specific, we first excluded the bad pixels, bad columns, and events with *ASCA* grades 1, 5 and 7. Next we carried out corrections for the gain, charge transfer inefficiency (for the observations performed after January 30, 2000), astrometry, and cosmic ray afterglow. By examining the light curve extracted in 0.5–12 keV from source-free regions or regions slightly affected by the sources, using **LC_CLEAN** scrip in Sherpa we identified and removed the data contaminated by occasional particle background flares during which the count rate is increased by 20% over the mean value. In addition to above, we masked all the point sources detected beyond the 3σ threshold in the ACIS images with CIAO tools **celldetect** and **wavdetect** (Freeman et al. 2002).

3. DATA ANALYSIS AND RESULTS

3.1. Background

In order to construct a local background template for each observation, we extract the spectrum from the boundary regions on the S3 CCD or I0-3 CCDs, where the influence of the thermal emission of the intracluster medium (ICM) is relatively weak, and fit the extracted spectrum with a model that consists of the ICM emission (a thermal APEC component absorbed by the Galactic column density given in Kalberla et al. 2005 and Dickey & Lockman 1990. The gas abundance is fixed to $0.3 Z_{\odot}$ if it is not well constrained), the Cosmic X-ray Background (CXB; a power-law component with $\Gamma = 1.4$, which is also absorbed by the Galactic column density; e.g., Mushotzky et al. 2000; Carter & Read 2007),

the Galactic emission (two APEC components with $kT = 0.2$ keV and 0.08 keV, respectively; e.g., Humphrey & Buote 2006; Gu et al. 2012), and the particle-induced hard component derived from the corresponding *Chandra* blanksky templates available at the *Chandra* Science Center. The background template for the observation (i.e., Galactic + CXB + particle components) can thus be determined when the best-fit is achieved. When the corresponding data are available, we have also compared the count rate of our background template calculated in $0.2 - 2$ keV, where the effect of the particle component is less significant, with that of the archive *ROSAT* All-Sky Survey (RASS) diffuse background maps, and obtained consistent results. It is difficult to estimate the field-to-field variations of both the Galactic and CXB background components in each observation. As an approximation in the analysis that follows we estimate the model parameter error ranges by taking into account both statistical and systematic uncertainties (10% as a conservative estimate; Kushino et al. 2002) in the background.

3.2. Imaging Spectroscopic Study of Gas Properties

3.2.1. Gas Temperature Distributions

For each observation we define 5 – 7 concentric annuli, which are all centered on the cluster’s X-ray peak. The width of each annulus is determined to guarantee a minimal photon count of 2500 cts in $0.7 - 7$ keV, and for the outermost annulus the condition that the photon count is at least twice the background should be satisfied simultaneously. We extract the *Chandra* ACIS S3 or I0-3 spectra from these concentric annuli, and fit them by using the X-ray spectral fitting package XSPEC v12.8.2 (Arnaud 1996). To minimize the effects of the instrumental background at higher energies and the calibration uncertainties at lower energies, we limit the fittings in $0.7 - 7$ keV. In the model fits, we estimate the influence of the outer spherical shells on the inner ones by using the XSPEC model PROJECT, and

fit the deprojected spectra with the optically thin, collisional plasma model APEC (Smith et al. 2001), which is absorbed by the foreground photoelectric absorption model WABS (the column density N_{H} is fixed to the corresponding Galactic value; see Kalberla et al. 2005 and Dickey & Lockman 1990). Whenever the gas metal abundance is not well constrained, we fix it to $0.3 Z_{\odot}$. We add an additional absorbed APEC component for the innermost annulus since it might be contaminated by the coexisting multi-phase gases (e.g., Makishima et al. 2001), if the F-test shows that the fitting is improved at the 90% confidence level. In this case the ICM temperature is defined as that of the hot phase. Smoothed gas temperature profiles, as well as the smoothed metal abundance profiles, are then derived by running cubic spline interpolation to the best-fit model parameters for the annulus set. Finally we calculate the average gas temperature of the cluster (Table 1) by fitting the spectra extracted between $0.2 - 0.5r_{500}$ (§3.2.3) using the same spectral model as above.

3.2.2. *X-Ray Surface Brightness Profiles and Gas Density Distributions*

We create the exposure map for each observed image by using the spectral weights calculated for an incident thermal gas spectrum that possesses the same average temperature and metal abundance as the cluster (§3.2.1). After the X-ray images are corrected by applying the exposure maps to remove the effects of vignetting and exposure time fluctuations, we use concentric annular bins, which are all centered at the X-ray peak of the gas halo, to extract the X-ray surface brightness profiles $S_X(R)$ (R is the two dimensional radius) in $0.7 - 7$ keV.

Under the assumptions of hydrodynamic equilibrium and spherical symmetry, the three-dimensional distribution of gas electron density n_e can be expressed with a β -model (e.g.,

Cavaliere & Fusco-Femiano 1976),

$$n_e(r) = n_0 \left[1 + \left(\frac{r}{r_c} \right)^2 \right]^{-3\beta/2}, \quad (1)$$

or a double- β model (e.g., Jones & Forman 1984)

$$n_e(r) = n_{0,1} \left[1 + \left(\frac{r}{r_{c,1}} \right)^2 \right]^{-3\beta_1/2} + n_{0,2} \left[1 + \left(\frac{r}{r_{c,2}} \right)^2 \right]^{-3\beta_2/2} \quad (2)$$

when a detectable central surface brightness excess appears in the inner regions, where r_c is the core radius and β is the slope. With the derived gas density profile and the profiles of gas temperature $T(r)$ and metal abundance $A(r)$, which are obtained in §3.2.1, we model the X-ray surface brightness profile as

$$S_X(R) = \int_R^\infty \Lambda(T, A) n_e n_p(r) \frac{r dr}{\sqrt{r^2 - R^2}} + S_{\text{bkg}}, \quad (3)$$

where S_{bkg} is the background, and $\Lambda(T, A)$ is the cooling function. The density $n_e(r)$ is determined when the best-fit to the observed surface brightness profile is achieved via χ^2 -test.

3.2.3. Characteristic Radius r_{500}

In order to derive the characteristic radius r_{500} , we first calculate the distribution of the total gravitating mass of the cluster in the regions covered by *Chandra*'s field of view under the hydro-statics equilibrium assumption

$$M(< r) = -\frac{r^2 k_b T_X}{G \mu m_p} \left[\frac{1}{T_X} \frac{dT_X}{dr} + \frac{1}{n_e} \frac{dn_e}{dr} \right], \quad (4)$$

where $\mu = 0.61$ is the mean molecular weight per hydrogen atom, k_b is the Boltzmann constant, and m_p is the proton mass. In the regions outside *Chandra*'s field of view, the mass profile $M(< r)$ is obtained by fitting the result derived above by applying the NFW

profile (Navarro et al. 1996)

$$\rho(r) = \frac{\rho_0}{(1 + r/r_s)^2 r/r_s}, \quad (5)$$

where $\rho(r)$ is the density of the total gravitating mass, and extrapolating the best-fit mass profile out to the point where the mean density of the enclosed gravitating mass is 500 times the critical density of the universe at the cluster’s redshift (Calculated M_{500} and r_{500} are listed in Table 1). The comparison of M_{500} between this and previous work (Zhao et al. 2015) was shown in Figure 1, the results are consistent with each other.

3.2.4. *SCC-WCC-NCC Classifications with Traditional Diagnostics*

Using the observed profiles of X-ray surface brightness, gas temperature, metal abundance and gas density, the clusters in our sample can be classified explicitly as an SCC, WCC, or NCC system coincidentally² with three frequently quoted traditional CC diagnostics, i.e., the central cooling time (CCT, Hudson et al. 2010)

$$t_{\text{cool}} \equiv \frac{5}{2} \frac{(n_e + n_i)kT}{n_e n_H \Lambda(T, A)} \quad \text{for } r < 0.048r_{500}, \quad (6)$$

cuspidity (Vikhlinin et al. 2007)

$$\alpha \equiv -\frac{d\log(n_e)}{d\log(r)} \quad \text{at } r = 0.04r_{500}, \quad (7)$$

and surface brightness concentration parameter (Santos et al. 2008)

$$C_{\text{SB}} \equiv \frac{\sum(r \leq 40\text{kpc})}{\sum(r \leq 400\text{kpc})}, \quad (8)$$

which is the ratio of the integrated surface brightnesses within central 40 kpc to that within 400 kpc. With these diagnostic parameters and the corresponding criteria listed in Table 2,

²In other words, a cluster is included in the sample only when the three traditional diagnostics give the same SCC/WCC/NCC classification

the sample clusters are classified as an SCC, WCC, or NCC system, as shown in column 8 before the slash mark in Table 3.

We find that in nine out of 12 SCC clusters the ratio of the central luminosity excess to the total luminosity integrated within $0.45r_{500}$ ($R_{\text{excess}} \equiv L_{\text{excess}}^{0.7-7\text{keV}}/L_{\text{total}}^{0.7-7\text{keV}}$) is significant, ranging from about 8% to 50% (Table 3). In seven out of nine WCC clusters a central surface brightness excess is detected, but the ratio R_{excess} is much lower (typically a few percent) except in A1651 ($\simeq 10\%$) and ESO306-G170B ($\simeq 21\%$). In NCC clusters the effect of the central luminosity excess, if it does exist, is actually negligible.

3.2.5. Power Spectra of the X-Ray Images

For each cluster we first calculate the two-dimensional Fourier transform of the background-subtracted and exposure-corrected X-ray image (i.e., the flux distribution $F(\vec{R})$), which is not smoothed, as

$$\tilde{F}(\vec{k}) = \int_S F(\vec{R}) e^{i\vec{R}\vec{k}} d\vec{R}, \quad (9)$$

where k is the wavenumber, and S represents the hole image by using the MATLAB tool `fft2` and `fftshift`. We removed all the point sources detected beyond 3σ threshold, and fill the corresponding regions via interpolation with neighboring pixels assuming Poisson statistics. The CCD gaps between the ACIS-I chips are filled in the same way. We find that the systematic errors introduced in the process are much smaller than the statistical errors, which will be estimated below, at wavenumbers that we are interested in ($0.2 \text{ kpc}^{-1} \leq k \leq 0.001 \text{ kpc}^{-1}$). The two-dimensional power spectrum is then obtained as

$$P(k) = \langle |\tilde{F}(\vec{k})|^2 \rangle, \quad (10)$$

Next, we create a random fluctuation distribution $F_{\text{err}}(\vec{R})$ for the observed image by running Monte-Carlo simulations to estimate the fluctuation on each pixel, which is assumed to

follow the Poisson distribution, and add the fluctuations map into the observed map to create a simulated image $F_{\text{sim}}(\vec{R})$ (i.e., $F(\vec{R}) + F_{\text{err}}(\vec{R})$). After 100 simulated images are randomly created, we calculate their power spectra and use the scatter of them to determine the error range of the image power spectrum $P(k)$ of the cluster. In the simulation we have added an additional 5% systematic error to account for the subtle numerical and instrumental effects (e.g., errors introduced by the gridding of image, the periodic boundary conditions, the inhomogeneity in the exposure between neighboring pixels, and the method of removing and filling point sources; Hudson et al. 2010). The obtained power spectra and the corresponding error ranges for the sample clusters are plotted in Figures 2.

We find that in the log-log space the derived image power spectra of 39 out of 41 sample clusters become flat as the wavenumbers increases and can be represented by a constant component when the wavenumber is large enough ($k \geq 0.01 - 0.05 \text{ kpc}^{-1}$ for 31 clusters, and $k \geq 0.05 - 0.1 \text{ kpc}^{-1}$ for seven clusters, $k \geq 0.1 \text{ kpc}^{-1}$ for one cluster), while at small wavenumbers a power excess beyond the constant component appears in all clusters, with a clear tendency that the power excess is stronger in CC clusters than in NCC clusters. This is very likely due to the fact that CC clusters usually harbor large bright cores (Vikhlinin et al. 2007; Santos et al. 2008), which may significantly enhance the power on scales comparable to the cooling radius ($r_{\text{cool}}, \sim 0.1r_{500}$ as shown in Table 3; cooling radius is the radius within which the gas cooling time is $< 7.7 \times 10^9 \text{ yr}$, the light travel time from $z = 1$; Rafferty et al. 2006). To illustrate this we plot the relative core brightness (defined as the ratio of integrated surface brightness within central $0.048r_{500}$ to that within $0.45r_{500}$) against the power ratio (defined as the ratio of power at $0.35r_{500}$ to that at large wavenumbers where image power spectra reduce to a constant component) which reflect the power excess we mentioned above in Figure 3, and find that there indeed exists an unambiguous correlation between the two parameters. We also have attempted to fit the observed power spectra by adding a β component into the model to represent the power excess, and find that in all

sample clusters the model (β +constant component) can provide an acceptable fitting to the power spectrum in the log-log space (Fig. 2). On the other hand, the model that consists of two β components always gives a relatively poor fit to the observed power spectrum in nearby all galaxy clusters.

In Figure 4 we plot the two-dimensional power spectra of the X-ray images of all sample clusters, together with the same power spectrum set scaled by r_{500} (x-axis) and the power at $0.01r_{500}$ (y-axis). In all cases the power spectra is truncated at five pixel^{-1} . In the figures we color-code the power spectra according to the classification based on the traditional cool core diagnostic parameters (i.e., central cooling time, cuspliness, and concentration parameter; see §3.2.4 and Table 2): blue for SCC clusters, green for WCC clusters, and red for NCC clusters. The errors are typically about 10% for small wavenumbers and 20% for large wavenumbers, which consistent with the errors of Zhuravleva et al. (2015) in the same scale (Zhuravleva et al. (2015) specifically studied Perseus cluster), and are not shown in the figures for a better visualization of the profiles. Despite the large scatter, we find that there are systematic distinctions between the shapes of the unscaled power spectra of SCC, WCC, and NCC systems. The distinctions become more obvious when we examine the scaled power spectra, which implies that the *Chandra* image power spectra may be used to classify galaxy clusters located with in $z \leq 0.5$ as CC or NCC systems, as will be discussed below.

4. DISCUSSION

In order to characterize the distinctions between the image power spectra of SCC, WCC, and NCC systems, for each cluster we locate two specific points on the line of the scaled power spectrum at wavenumbers $k = 1/0.35$ and $1/0.035$, which correspond to the scales of $0.35r_{500}$ and $0.035r_{500}$ in the real image space, respectively, and use the two points as the

left-top and right-bottom vertices to determine a rectangular box (Fig. 5)³. Using this box we introduce a new CC diagnostic parameter, i.e., the power excess index (PEI), to quantify the degree of the power excess as $\Delta_{\text{PE}} \equiv A_{\text{below}}/(A_{\text{below}} + A_{\text{above}})$, where A_{below} and A_{above} denote the box areas below and above the line of the power spectrum, respectively. The CC diagnostic defined in such a way shows several potential advantages over its counterparts, which may be helpful in future large surveys such as e-ROSITA. For example, the application of PEI is free of the effects of centroid shift of the X-ray halo caused by merger event, which may make the determination of centroid of the X-ray gas halo ambiguous⁴, and the corresponding calculation is straightforward, almost irrelevant to the complicated spectral analysis. We then classify the clusters in our sample with the new diagnostic parameter and the corresponding criteria listed in Table 2, and show the results in Figure 6. We find that our classification agrees very well with those achieved with the traditional CC diagnostics, which are also displayed in Figure 6, except for the cases of A2319, A2667, and ZwCl0015. Possible reasons for the differences in classification are discussed below.

A2319 — This is a nearby, massive merging system showing a huge radio halo that extends out to about $35'$ (~ 2 Mpc; Storm et al. 2015 and references therein). By examining the *Chandra* image we find that the core region of the cluster is loose, flat, but well developed with distinct boundaries. In addition to this the core also shows a hierarchical structure with one flat core embedded in another. Using the PEI diagnostic, which is sensitive to such imaging substructures, we classify the cluster as a WCC system. This is supported by the results of O’Hara et al. (2004), who revealed a relatively weak cool gas clump slightly

³The positions of the points are chosen to cover the range where the observed power spectrum turns to be flat as the wavenumber increases

⁴In such a case the calculation of PEI can be performed immediately after a rough estimate of r_{500} is given by, e.g., the r_{500} -temperature/luminosity scaling relations (Sun et al. 2009)

south of the X-ray peak on the *Chandra* temperature map and identified it as a previously unknown cool core. On the other hand we find that, because the gas temperature is high and the core is loose, comparing with typical WCC clusters A2319 tends to possess a longer central cooling time and a lower concentration parameter. This is why it is classified as an NCC cluster with traditional CC diagnostics.

A2667 — We classify this luminous cluster as an SCC system using the PEI diagnostic, and this is supported by the drastic gas temperature drop detected in the central 100 kpc in our deprojected spectral analysis (Fig. 7). Previous *ROSAT* observation indicated that the cluster shows strong evidence for a cooling core (Rizza et al. 1998), which is supported by the appearance of strong H_α and $[\text{O II}]\lambda 3727$ lines from the central dominating galaxy (Rizza et al. 1998). Note that, using the central cooling time and concentration diagnostics the cluster can be classified as an SCC system marginally (1σ confidence level), while using the cuspsiness diagnostic the cluster is classified as a WCC system (close to an NCC system).

ZwCl0015 — This cluster is less studied in literature compared with the above two Abell systems. On its *Chandra* image we find that, although the emission from the core region is sharply peaked, which leads to a lower central cooling time and slightly higher surface brightness concentration than typical NCC clusters, the X-ray emission from the core is apparently weaker than most WCC clusters. Moreover the gas temperature profile of this cluster shows very mild spatial variations and is actually consistent with a constant distribution (Fig. 7). Due to these facts the cluster is classified as an NCC system using the PEI diagnostic, instead of a WCC classification suggested by the traditional CC diagnostics.

In order to investigate whether or not the PEI diagnostic is applicable to clusters located within $z \simeq 0.5$ or even at higher redshifts, we select three CC clusters (A1068, A1664 and RXCJ2014.8-2430), WCC (A2667, A795, and A963), and NCC (A2104, A2443, AC114) clusters respectively, each possessing an intermediate appearance in its own classification, as

the templates, and create the corresponding simulated clusters that are located at $z = 0.5$, 0.6 , and 0.7 , by cloning the three template clusters under the assumption of non-evolution. In the process of cloning we have assumed a typical 50 ks of *Chandra* or *XMM-Newton* exposure, and have taken into account the effects caused by the changes of angular and luminosity distances (see Santos et al. 2008 for more details of this approach and Bouwens et al. 1998 for the original application in the optical band). We find that, if spatial resolution and signal-to-noise ratios that can be achieved in typical *Chandra* or *XMM-Newton* observations are assumed, the PEI diagnostic can work well at $z = 0.5$ if the flux of the simulated cluster is no less than $\simeq 2.8 \times 10^{-13} \text{ erg cm}^{-2} \text{ s}^{-1}$ for *Chandra* or $\simeq 1.6 \times 10^{-13} \text{ erg cm}^{-2} \text{ s}^{-1}$ for *XMM-Newton*, which roughly correspond to intermediately sized clusters with a gas temperature of $\sim 3 \text{ keV}$. The comparison between the PEI classifications of the simulated clusters and the PEI classifications of the origin ones was shown in Figure 8. For simulated clusters located at $z = 0.6$ the PEI diagnostic fails in about 20% cases due to the limited signal-to-noise ratio and spatial resolution of a typical *Chandra/XMM-Newton* observation. Based on these results, we conclude that with current *Chandra* and *XMM-Newton* data, the new diagnostic can be safely applied to at least intermediate redshifts as a useful complement to the traditional diagnostics, and to even higher redshifts with higher quality data provided by future missions.

It is worth noting that the power excess begins at $k \lesssim 0.01 - 0.05 \text{ kpc}^{-1}$ in 31 clusters (76% of the sample), and at $k \lesssim 0.05 - 0.1 \text{ kpc}^{-1}$ for seven clusters (17%). These correspond to $\gtrsim 20 - 100 \text{ kpc}$ or $\gtrsim 10 - 20 \text{ kpc}$ in real space, scales at which the fluctuations of X-ray surface brightness, gas density, and velocity were found (e.g., Walker et al. 2015, Churazov et al. 2012, Zhuravleva et al. 2015, Rebusco et al. 2005, Rebusco et al. 2006). The fluctuations, which are speculated to be caused by either AGN feedback, or merger, or both, may contribute part of the power excess but not all, since the fluctuations should be detected at relatively low levels compared with the significance of the power excess ($\simeq 1$ magnitude

for SCC, $\lesssim 0.5$ magnitude for WCC at 50 kpc, $\simeq 0.5$ magnitude for NCC at 200 kpc). To further evaluate this, we have attempted to use a two-dimensional β or 2β model, which is spatially smoothed, to approximate the emission distribution of the sample clusters. We find that the power spectra calculated from the modeled clusters show similar power excess as observed. Despite this, to quantitatively answer the question about how much the gas fluctuations contribute to the observed power excess still remains an interesting task in the future.

5. SUMMARY

We propose a new CC diagnostic based on the study of the two-dimensional power spectra of the *Chandra* X-ray images of 41 galaxy clusters ($z = 0.01 \sim 0.54$). By calculating the power excess index we find that the CC-NCC classification based on our new diagnostic agrees very well with those obtained by the traditional CC diagnostics. The new diagnostic can be safely applied to at least intermediate redshifts as a useful complement to the traditional diagnostics.

This work was supported by the Ministry of Science and Technology of China (grant No. 2013CB837900), the National Science Foundation of China (grant Nos. 11125313, 11203017, 11433002, 61271349, and 61371147), the Chinese Academy of Sciences (grant No. KJZD-EW-T01), and Science and Technology Commission of Shanghai Municipality (grant No. 11DZ2260700).

Table 1. Basic Properties of Sample Clusters.

Name	ObsID ^a	R.A.	Dec.	z	$T_{\text{avg}}^{\text{b}}$	M_{500}	r_{500}
		(J2000)	(J2000)		(keV)	($10^{14} M_{\odot}$)	(kpc)
A0193	6931	01:25:07.3	+08:41:36.00	0.0486	$3.83^{+0.18}_{-0.18}$	$1.66^{+0.90}_{-0.28}$	816^{+127}_{-50}
A0520	4215	04:54:09.7	+02:55:23.41	0.1990	$9.04^{+0.08}_{-0.08}$	$6.78^{+0.74}_{-0.48}$	1246^{+44}_{-30}
A0697	4217	08:42:53.3	+36:20:12.00	0.2820	$12.43^{+1.31}_{-1.34}$	$11.34^{+6.04}_{-3.86}$	1439^{+220}_{-186}
A0795	11734	09:24:05.3	+14:10:21.00	0.1359	$5.09^{+0.27}_{-0.27}$	$2.64^{+0.36}_{-0.52}$	928^{+41}_{-66}
A0963	903	10:17:03.4	+39:02:53.66	0.2060	$6.59^{+0.28}_{-0.27}$	$4.20^{+0.66}_{-0.45}$	1060^{+53}_{-38}
A0970	12285	10:17:34.3	−10:42:01.00	0.0587	$4.18^{+0.39}_{-0.39}$	$5.94^{+7.75}_{-2.07}$	1245^{+399}_{-166}
A1068	1652	10:40:44.5	+39:57:11.07	0.1375	$5.07^{+0.24}_{-0.24}$	$3.33^{+0.45}_{-0.39}$	1003^{+41}_{-50}
A1204	2205	11:13:20.4	+17:35:40.93	0.1706	$4.56^{+0.35}_{-0.32}$	$2.09^{+0.13}_{-0.28}$	850^{+17}_{-39}
A1651	4185	12:59:22.3	−04:11:44.87	0.0850	$6.50^{+0.32}_{-0.33}$	$6.79^{+2.04}_{-1.71}$	1293^{+118}_{-120}
A1664	7901	13:03:42.4	−24:14:43.66	0.1283	$5.35^{+0.26}_{-0.20}$	$3.79^{+0.40}_{-0.38}$	1050^{+36}_{-38}
A1736	4186	13:26:52.1	−27:06:33.00	0.0458	$2.60^{+0.07}_{-0.08}$	$1.98^{+0.60}_{-0.73}$	866^{+80}_{-123}
A1991	3193	14:54:31.5	+18:38:32.94	0.0587	$2.64^{+0.07}_{-0.07}$	$0.90^{+0.04}_{-0.07}$	664^{+9}_{-18}
A2034	12886	15:10:13.1	+33:31:41.00	0.1130	$8.96^{+0.32}_{-0.32}$	$8.24^{+1.20}_{-0.35}$	1367^{+63}_{-20}
A2061	10449	15:21:15.3	+30:39:17.00	0.0784	$5.05^{+0.17}_{-0.17}$	$3.63^{+1.73}_{-0.52}$	1051^{+146}_{-51}
A2104	895	15:40:06.8	−03:17:39.00	0.1533	$9.24^{+0.49}_{-0.49}$	$5.45^{+0.68}_{-0.47}$	1176^{+47}_{-35}
A2163	1653	16:15:34.1	−06:07:26.00	0.2030	$16.09^{+0.52}_{-0.53}$	$19.49^{+2.07}_{-2.51}$	1770^{+61}_{-79}
A2255	894	17:12:31.0	+64:05:33.00	0.0806	$6.64^{+0.14}_{-0.14}$	$4.23^{+0.81}_{-0.48}$	1105^{+66}_{-44}
A2319	3231	19:20:45.3	+43:57:43.00	0.0557	$10.17^{+0.32}_{-0.32}$	$11.50^{+3.07}_{-4.75}$	1554^{+127}_{-253}
A2443	12257	22:25:07.4	+17:20:17.00	0.1080	$5.93^{+0.49}_{-0.49}$	$4.25^{+2.43}_{-1.01}$	1097^{+178}_{-94}
A2554	1696	23:12:15.1	−21:33:56.00	0.1108	$4.54^{+0.41}_{-0.34}$	$1.83^{+0.30}_{-0.32}$	828^{+43}_{-52}

Table 1—Continued

Name	ObsID ^a	R.A.	Dec.	z	$T_{\text{avg}}^{\text{b}}$	M_{500}	r_{500}
		(J2000)	(J2000)		(keV)	($10^{14} M_{\odot}$)	(kpc)
A2657	4941	23:44:56.3	+09:11:24.00	0.0402	$3.99^{+0.12}_{-0.12}$	$2.41^{+1.59}_{-0.90}$	927^{+171}_{-135}
A2667	2214	23:51:39.3	−26:05:03.22	0.2300	$7.97^{+0.89}_{-0.74}$	$6.51^{+2.52}_{-1.75}$	1217^{+140}_{-120}
A3158	3712	03:42:39.6	−53:37:50.00	0.0597	$4.96^{+0.09}_{-0.09}$	$3.22^{+0.50}_{-0.37}$	1016^{+49}_{-41}
A3364	9419	05:47:34.2	−31:53:01.00	0.1483	$7.41^{+0.57}_{-0.57}$	$4.83^{+1.19}_{-1.13}$	1131^{+86}_{-96}
A3376	3202	06:02:10.1	−39:57:22.31	0.0456	$4.37^{+0.14}_{-0.11}$	$3.35^{+0.85}_{-0.58}$	1033^{+81}_{-62}
A3391	4943	06:26:15.4	−53:40:52.00	0.0514	$4.88^{+0.20}_{-0.21}$	$2.27^{+0.74}_{-0.43}$	905^{+89}_{-62}
A3395SW	4944	06:26:48.0	−54:32:43.00	0.0510	$4.71^{+0.24}_{-0.23}$	$2.10^{+0.56}_{-0.27}$	883^{+73}_{-39}
A3822	8269	21:54:06.2	−57:50:49.00	0.0759	$5.20^{+0.26}_{-0.25}$	$3.37^{+0.62}_{-0.49}$	1026^{+59}_{-52}
AC114	1562	22:58:52.3	−34:46:55.00	0.3120	$7.38^{+0.38}_{-0.38}$	$3.33^{+0.17}_{-0.18}$	947^{+15}_{-17}
ESO306-G170B	3188	05:40:06.4	−40:50:08.73	0.0358	$2.66^{+0.13}_{-0.11}$	$0.87^{+0.21}_{-0.14}$	662^{+50}_{-36}
IC1262	7322	17:33:02.8	+43:45:44.07	0.0344	$2.28^{+0.07}_{-0.07}$	$0.43^{+0.05}_{-0.03}$	522^{+18}_{-12}
MACSJ2211.7-0349	3284	22:11:44.6	−03:49:47.00	0.2700	$14.93^{+2.81}_{-2.32}$	$9.32^{+1.19}_{-0.92}$	1354^{+56}_{-46}
NGC1550	3186	04:19:37.9	+02:24:31.95	0.0120	$1.27^{+0.02}_{-0.03}$	$0.26^{+0.10}_{-0.03}$	446^{+51}_{-15}
PKS0745-19	6103	07:47:31.4	−19:17:42.29	0.1028	$8.93^{+0.66}_{-0.51}$	$7.11^{+0.72}_{-0.56}$	1305^{+43}_{-35}
RBS797	7902	09:47:12.8	+76:23:13.77	0.3540	$9.69^{+0.82}_{-0.83}$	$6.45^{+1.50}_{-1.29}$	1164^{+84}_{-84}
RXCJ1524-3154	9401	15:24:12.9	−31:54:21.99	0.1028	$4.22^{+0.22}_{-0.16}$	$3.13^{+0.35}_{-0.38}$	993^{+35}_{-42}
RXCJ2014.8-2430	11757	20:14:51.6	−24:30:22.52	0.1612	$7.14^{+0.44}_{-0.40}$	$4.15^{+0.51}_{-0.40}$	1072^{+42}_{-35}
RXJ1423.8+2404	4195	14:23:47.9	+24:04:42.37	0.5431	$7.67^{+0.51}_{-0.51}$	$3.76^{+0.69}_{-0.80}$	907^{+52}_{-69}
Zw3146	909	10:23:39.6	+04:11:11.90	0.2906	$9.26^{+0.62}_{-0.61}$	$6.64^{+0.97}_{-0.55}$	1200^{+56}_{-34}
ZwCl0015	12251	00:06:20.6	+10:51:52.98	0.1675	$6.85^{+0.53}_{-0.36}$	$2.83^{+0.28}_{-0.42}$	941^{+30}_{-48}

Table 1—Continued

Name	ObsID ^a	R.A.	Dec.	z	$T_{\text{avg}}^{\text{b}}$	M_{500}	r_{500}
		(J2000)	(J2000)		(keV)	($10^{14} \text{ M}_{\odot}$)	(kpc)
ZwCl2089	10463	09:00:36.9	+20:53:40.27	0.2400	$4.60^{+0.34}_{-0.32}$	$2.50^{+0.35}_{-0.34}$	882^{+39}_{-42}

^aOnly one time observation is used for each cluster, which has the best signal to noise ratio and the minimum offset.

^bAverage temperature is calculated for $0.2 - 0.5 \text{ } r_{500}$.

Table 2: Three traditional cool core diagnostics and the new one (i.e., PEI) introduced in this work.

Category	CCT	Cuspiness	Concentration	PEI
	$t_{\text{cool}} (h_{71}^{-1/2} \text{ Gyr})$	α	C_{SB}	Δ_{PE}
SCC	< 1	> 0.75	> 0.155	> 0.42
WCC	$1 - 7.7$	$0.5 - 0.75$	$0.075 - 0.155$	$0.31 - 0.42$
NCC	> 7.7	< 0.5	< 0.075	< 0.31

Table 3. Classifications of sample clusters with both the three traditional diagnostics (coincidentally) and the new CC diagnostic.

Name ¹	t_{cool}^2 ($h_{71}^{-1/2}$ Gyr)	α^3	C_{SB}^4	r_{cool}^5 (kpc)	Δ_{PE}^6	R_{excess}^7 (%)	Category ⁸
A0193	$12.22^{+2.27}_{-2.31}$	$0.23^{+0.03}_{-0.01}$	$0.047^{+0.003}_{-0.002}$	$14.9^{+9.1}_{-6.4}$	0.24 ± 0.03	1.9 ± 0.5	NCC/NCC
A0520	$8.04^{+2.21}_{-2.22}$	$0.03^{+0.00}_{-0.00}$	$0.016^{+0.003}_{-0.002}$	—	0.27 ± 0.04	—	NCC/NCC
A0697	$11.04^{+3.02}_{-4.62}$	$0.20^{+0.02}_{-0.03}$	$0.035^{+0.002}_{-0.003}$	—	0.17 ± 0.05	—	NCC/NCC
A0795	$3.87^{+0.42}_{-0.74}$	$0.68^{+0.02}_{-0.04}$	$0.120^{+0.006}_{-0.005}$	$83.6^{+13.5}_{-7.2}$	0.38 ± 0.02	—	WCC/WCC
A0963	$2.32^{+0.27}_{-0.29}$	$0.52^{+0.03}_{-0.03}$	$0.098^{+0.005}_{-0.005}$	$88.1^{+12.2}_{-9.9}$	0.36 ± 0.02	1.7 ± 0.2	WCC/WCC
A0970	$15.45^{+3.47}_{-4.44}$	$0.20^{+0.03}_{-0.02}$	$0.041^{+0.003}_{-0.003}$	—	0.26 ± 0.06	—	NCC/NCC
A1068	$0.91^{+0.06}_{-0.07}$	$1.09^{+0.03}_{-0.04}$	$0.281^{+0.011}_{-0.010}$	$109.4^{+4.4}_{-5.3}$	0.56 ± 0.01	45.7 ± 21.9	SCC/SCC
A1204	$0.75^{+0.07}_{-0.08}$	$1.12^{+0.02}_{-0.04}$	$0.328^{+0.013}_{-0.013}$	$111.6^{+8.0}_{-5.4}$	0.43 ± 0.02	—	SCC/SCC
A1651	$3.06^{+0.60}_{-0.60}$	$0.70^{+0.05}_{-0.06}$	$0.076^{+0.004}_{-0.004}$	$66.8^{+18.9}_{-14.7}$	0.34 ± 0.03	10.2 ± 1.7	WCC/WCC
A1664	$0.99^{+0.06}_{-0.07}$	$1.14^{+0.03}_{-0.04}$	$0.209^{+0.008}_{-0.008}$	$93.4^{+3.8}_{-3.6}$	0.52 ± 0.01	15.3 ± 2.7	SCC/SCC
A1736	$24.62^{+6.50}_{-10.89}$	$0.15^{+0.01}_{-0.03}$	$0.022^{+0.002}_{-0.002}$	—	0.22 ± 0.08	1.2 ± 0.3	NCC/NCC
A1991	$0.67^{+0.01}_{-0.02}$	$1.16^{+0.01}_{-0.03}$	$0.204^{+0.007}_{-0.007}$	$67.3^{+1.4}_{-1.3}$	0.56 ± 0.01	50.4 ± 11.7	SCC/SCC
A2034	$19.79^{+2.97}_{-3.09}$	$0.12^{+0.01}_{-0.00}$	$0.030^{+0.001}_{-0.002}$	—	0.25 ± 0.02	0.3 ± 0.0	NCC/NCC
A2061	$27.75^{+10.82}_{-11.16}$	$0.03^{+0.01}_{-0.01}$	$0.016^{+0.002}_{-0.002}$	—	0.16 ± 0.09	—	NCC/NCC
A2104	$27.77^{+4.58}_{-5.75}$	$0.12^{+0.00}_{-0.00}$	$0.040^{+0.002}_{-0.002}$	$9.5^{+8.1}_{-9.5}$	0.26 ± 0.03	0.5 ± 0.1	NCC/NCC
A2163	$14.36^{+1.25}_{-2.04}$	$0.15^{+0.01}_{-0.01}$	$0.023^{+0.001}_{-0.001}$	—	0.23 ± 0.02	—	NCC/NCC
A2255	$28.27^{+3.81}_{-6.21}$	$0.09^{+0.01}_{-0.01}$	$0.019^{+0.001}_{-0.001}$	—	0.18 ± 0.06	—	NCC/NCC
A2319	$13.40^{+1.39}_{-4.11}$	$0.46^{+0.02}_{-0.07}$	$0.043^{+0.002}_{-0.002}$	—	0.35 ± 0.04	0.8 ± 0.1	NCC/WCC
A2443	$14.51^{+5.54}_{-6.38}$	$0.16^{+0.02}_{-0.01}$	$0.043^{+0.003}_{-0.003}$	—	0.24 ± 0.04	—	NCC/NCC
A2554	$11.87^{+2.20}_{-3.12}$	$0.20^{+0.01}_{-0.01}$	$0.066^{+0.004}_{-0.004}$	—	0.21 ± 0.03	1.1 ± 0.3	NCC/NCC
A2657	$3.33^{+0.84}_{-0.79}$	$0.61^{+0.12}_{-0.11}$	$0.077^{+0.004}_{-0.003}$	$38.2^{+14.9}_{-12.6}$	0.35 ± 0.03	1.0 ± 0.1	WCC/WCC
A2667	$1.20^{+0.18}_{-0.18}$	$0.54^{+0.03}_{-0.04}$	$0.152^{+0.007}_{-0.008}$	$135.9^{+14.2}_{-12.9}$	0.47 ± 0.02	4.5 ± 0.5	WCC/SCC
A3158	$11.27^{+1.28}_{-1.54}$	$0.29^{+0.02}_{-0.01}$	$0.041^{+0.002}_{-0.002}$	$24.8^{+7.0}_{-3.9}$	0.25 ± 0.02	0.1 ± 0.0	NCC/NCC
A3364	$13.19^{+3.77}_{-5.65}$	$0.14^{+0.01}_{-0.01}$	$0.040^{+0.003}_{-0.004}$	$13.5^{+46.4}_{-13.5}$	0.17 ± 0.04	—	NCC/NCC

Table 3—Continued

Name ¹	t_{cool}^2 ($h_{71}^{-1/2}$ Gyr)	α^3	C_{SB}^4	r_{cool}^5 (kpc)	Δ_{PE}^6	R_{excess}^7 (%)	Category ⁸
A3376	$9.44^{+1.10}_{-0.94}$	$0.27^{+0.01}_{-0.01}$	$0.027^{+0.002}_{-0.002}$	—	0.29 ± 0.03	—	NCC/NCC
A3391	$24.47^{+6.87}_{-7.37}$	$0.14^{+0.01}_{-0.01}$	$0.037^{+0.002}_{-0.002}$	—	0.19 ± 0.05	0.7 ± 0.2	NCC/NCC
A3395SW	$20.14^{+2.56}_{-3.74}$	$0.31^{+0.01}_{-0.02}$	$0.039^{+0.002}_{-0.003}$	—	0.18 ± 0.04	—	NCC/NCC
A3822	$9.56^{+2.21}_{-2.51}$	$0.39^{+0.04}_{-0.03}$	$0.037^{+0.003}_{-0.002}$	$38.9^{+15.1}_{-9.5}$	0.14 ± 0.05	—	NCC/NCC
AC114	$10.71^{+1.39}_{-1.68}$	$0.15^{+0.00}_{-0.01}$	$0.034^{+0.002}_{-0.002}$	—	0.18 ± 0.04	—	NCC/NCC
ESO306-G170B	$2.02^{+0.34}_{-0.26}$	$0.52^{+0.05}_{-0.03}$	$0.125^{+0.006}_{-0.006}$	$45.9^{+6.9}_{-7.5}$	0.40 ± 0.02	20.7 ± 2.7	WCC/WCC
IC1262	$1.15^{+0.08}_{-0.06}$	$0.69^{+0.03}_{-0.02}$	$0.127^{+0.005}_{-0.005}$	$49.1^{+2.0}_{-2.8}$	0.40 ± 0.03	4.9 ± 0.6	WCC/WCC
MACSJ2211.7-0349	$6.28^{+1.39}_{-1.71}$	$0.71^{+0.04}_{-0.04}$	$0.129^{+0.007}_{-0.007}$	$81.7^{+24.1}_{-15.4}$	0.39 ± 0.02	—	WCC/WCC
NGC1550	$0.95^{+0.04}_{-0.04}$	$0.97^{+0.03}_{-0.02}$	$0.232^{+0.008}_{-0.008}$	$33.0^{+1.0}_{-1.6}$	0.56 ± 0.06	19.5 ± 3.4	SCC/SCC
PKS0745-19	$1.00^{+0.06}_{-0.07}$	$1.41^{+0.02}_{-0.04}$	$0.204^{+0.008}_{-0.007}$	$104.6^{+5.3}_{-4.1}$	0.56 ± 0.01	13.9 ± 1.0	SCC/SCC
RBS797	$0.86^{+0.10}_{-0.10}$	$1.20^{+0.07}_{-0.07}$	$0.286^{+0.010}_{-0.011}$	$138.1^{+10.0}_{-8.0}$	0.49 ± 0.01	—	SCC/SCC
RXCJ1524-3154	$0.88^{+0.06}_{-0.06}$	$1.80^{+0.07}_{-0.06}$	$0.321^{+0.011}_{-0.011}$	$79.1^{+3.2}_{-3.1}$	0.61 ± 0.01	—	SCC/SCC
RXCJ2014.8-2430	$0.74^{+0.06}_{-0.05}$	$1.76^{+0.07}_{-0.05}$	$0.296^{+0.011}_{-0.011}$	$104.5^{+5.3}_{-6.1}$	0.63 ± 0.01	37.5 ± 2.0	SCC/SCC
RXJ1423.8+2404	$0.87^{+0.08}_{-0.11}$	$1.71^{+0.07}_{-0.12}$	$0.298^{+0.012}_{-0.013}$	$114.6^{+10.7}_{-6.6}$	0.44 ± 0.02	26.1 ± 3.6	SCC/SCC
Zw3146	$0.94^{+0.07}_{-0.06}$	$0.98^{+0.02}_{-0.02}$	$0.207^{+0.008}_{-0.008}$	$143.0^{+5.8}_{-6.9}$	0.55 ± 0.01	7.6 ± 0.5	SCC/SCC
ZwCl0015	$2.91^{+0.32}_{-0.33}$	$0.61^{+0.03}_{-0.03}$	$0.082^{+0.005}_{-0.005}$	$49.1^{+7.3}_{-6.0}$	0.25 ± 0.04	4.1 ± 0.7	WCC/NCC
ZwCl2089	$0.79^{+0.11}_{-0.11}$	$1.02^{+0.04}_{-0.04}$	$0.308^{+0.013}_{-0.012}$	$113.8^{+10.7}_{-8.7}$	0.53 ± 0.02	23.1 ± 4.4	SCC/SCC

Note. — (1) cluster name, (2) central cooling time (CCT, defined at $0.048r_{500}$), (3) cuspidity, (4) surface brightness concentration, (5) cooling radius, (6) power excess index (PEI), (7) the ratio of the central luminosity excess to the total luminosity (§3.2.2), (8) classification based on the three traditional diagnostics (coincidentally) and the new PEI (see §3.2.4 and §4 for details).

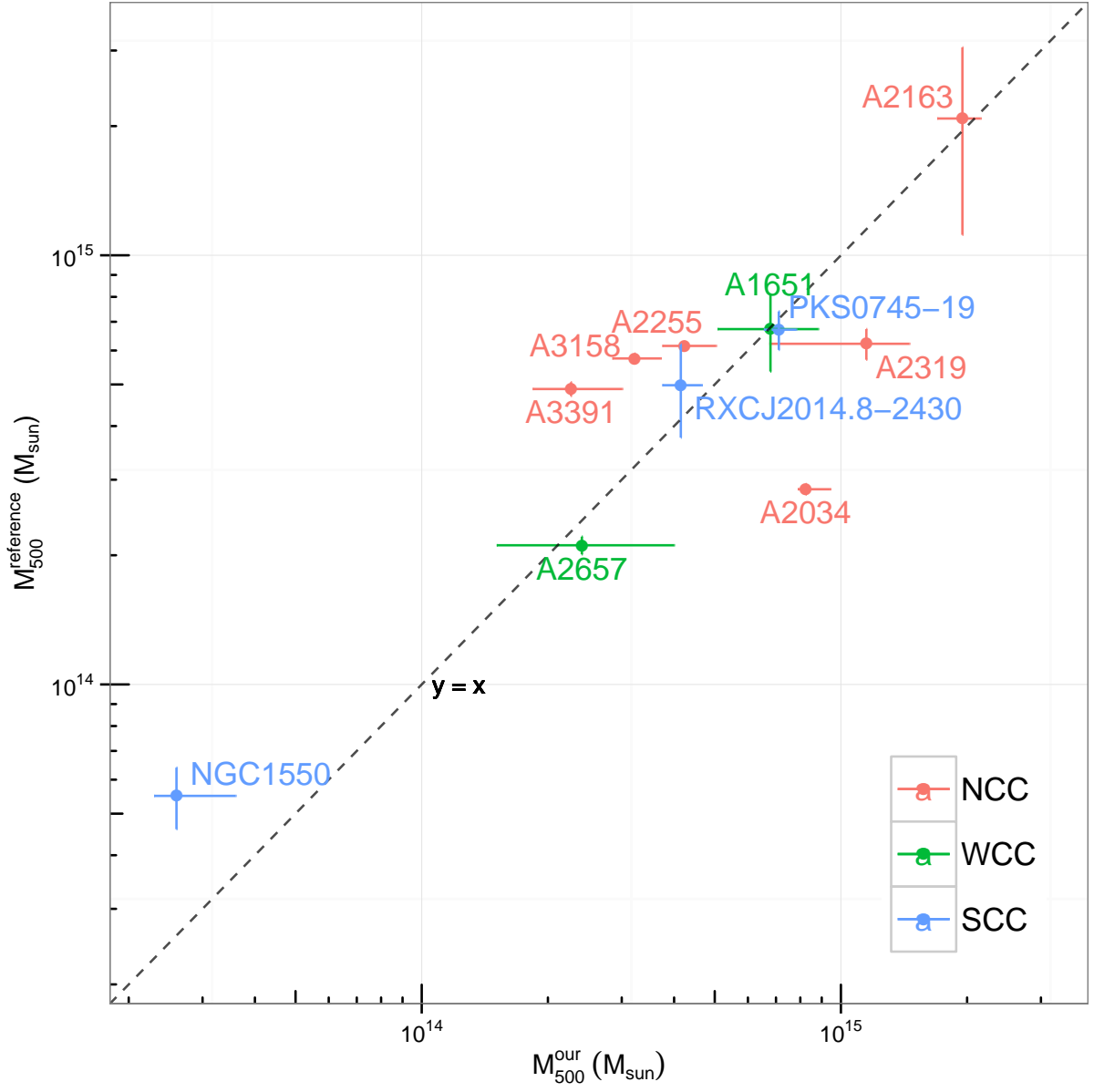
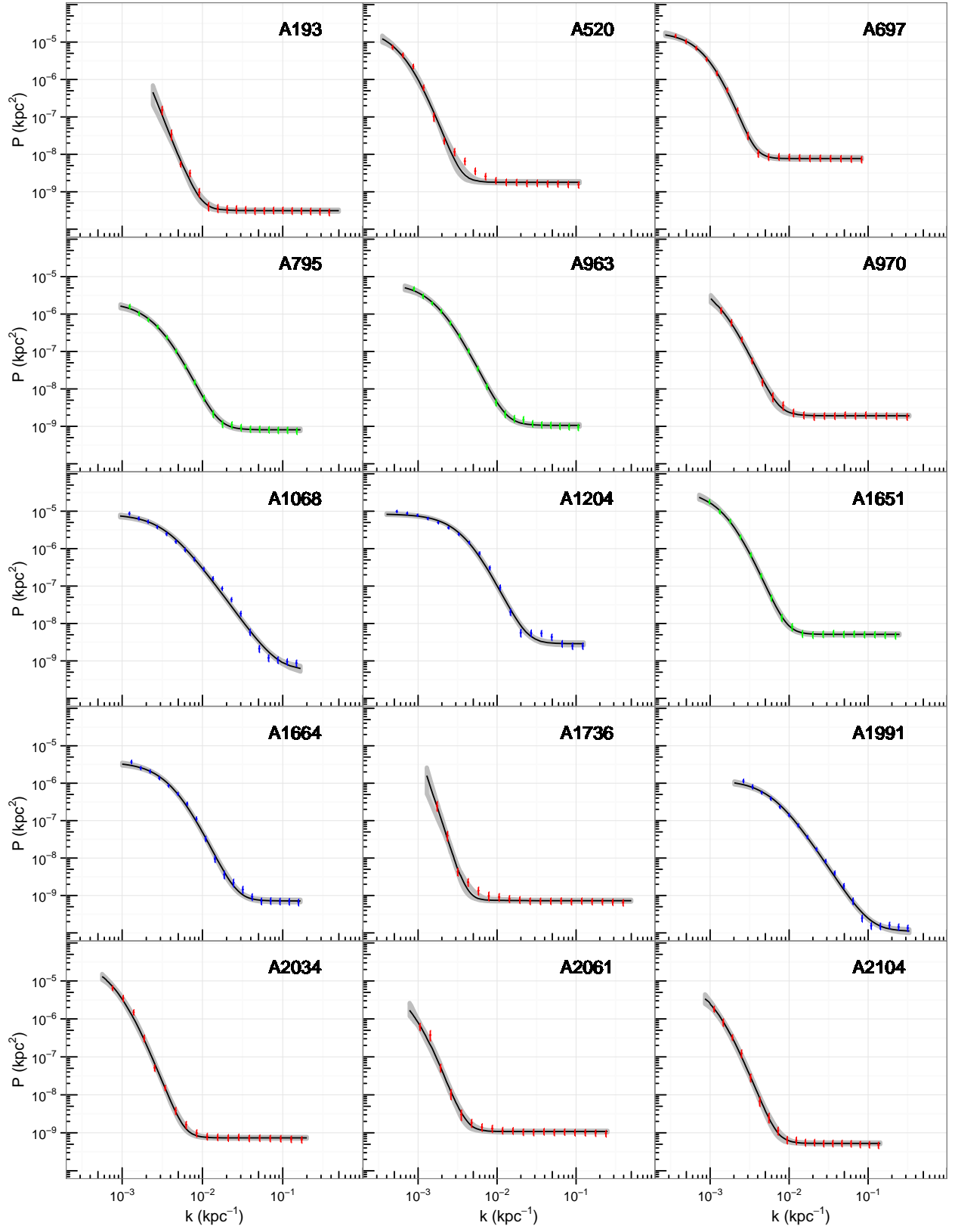
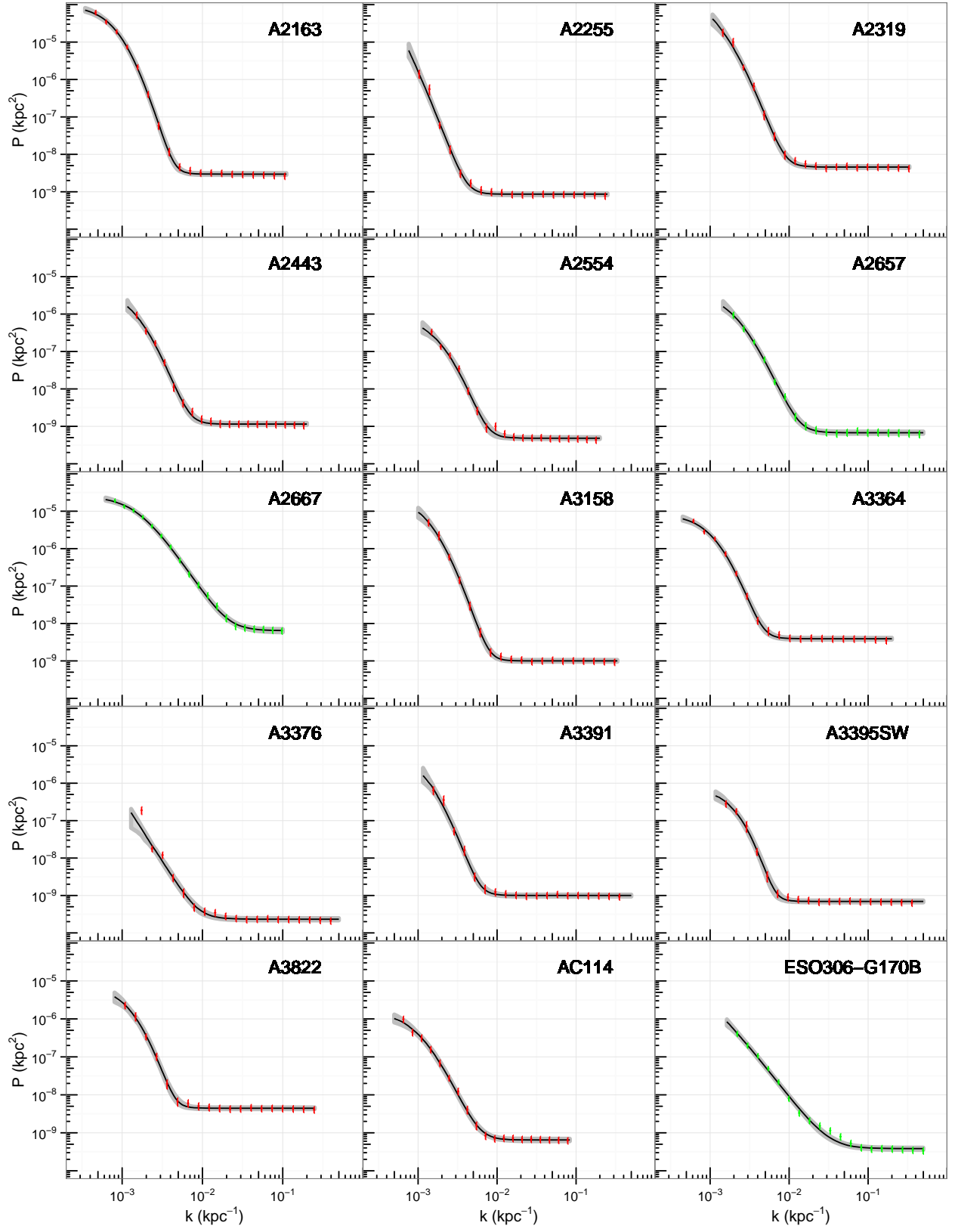


Fig. 1.— Comparison the calculated M_{500} between this work and previous work (Zhao et al. 2015).





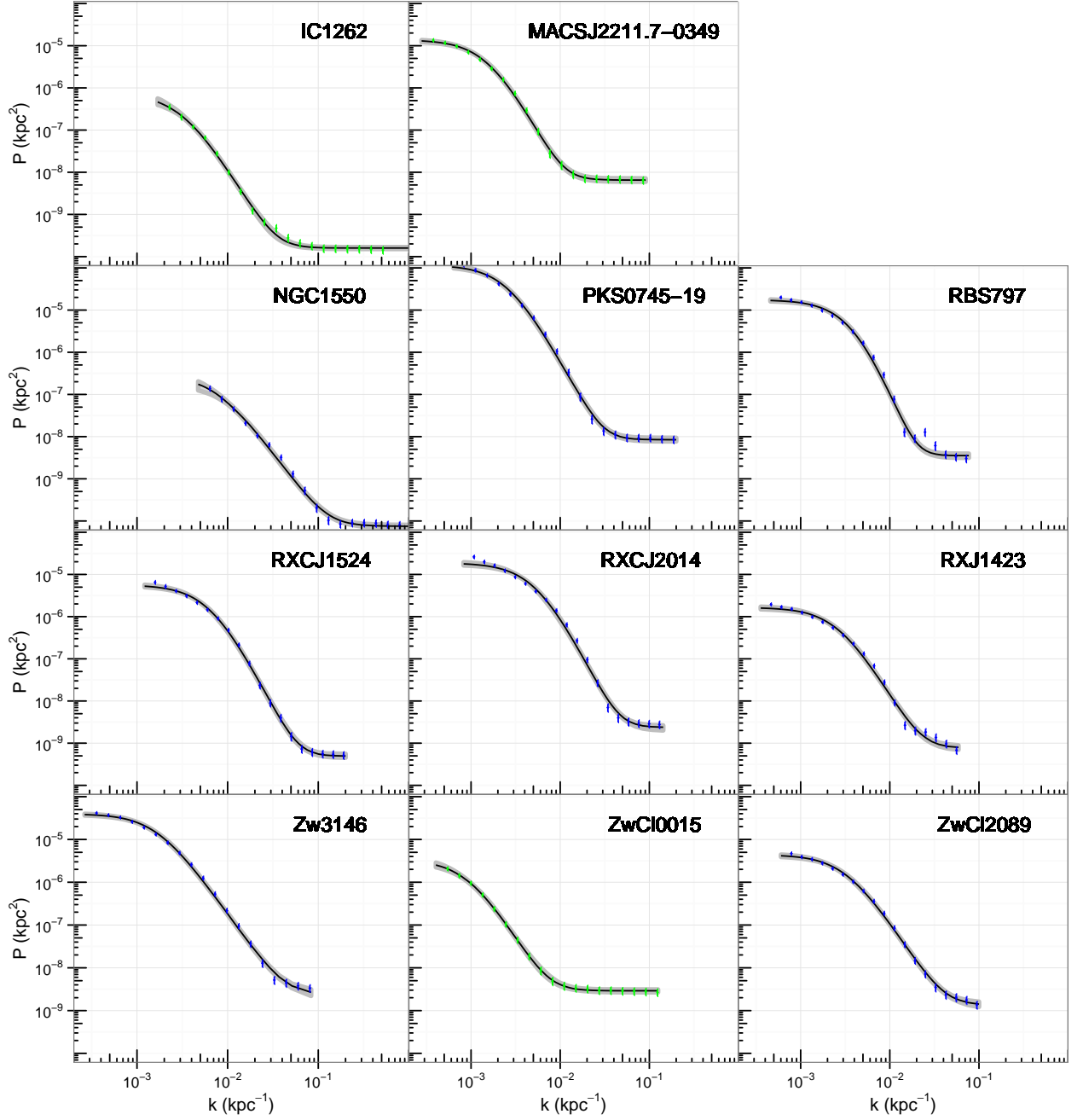


Fig. 2.— Observed power spectra of each cluster with the best-fit model ($\beta + \text{constant}$ component) and the corresponding confidence band, which are marked in black solid line and gray shade, respectively. The cluster categories are represented with different colors, We present the SCC's in blue, WCC's in green, and NCC's in red. It should be noted that the power error bars in small wavenumber range cannot be well visualized due to the logarithmic axes, though their relative errors are typically about 10%.

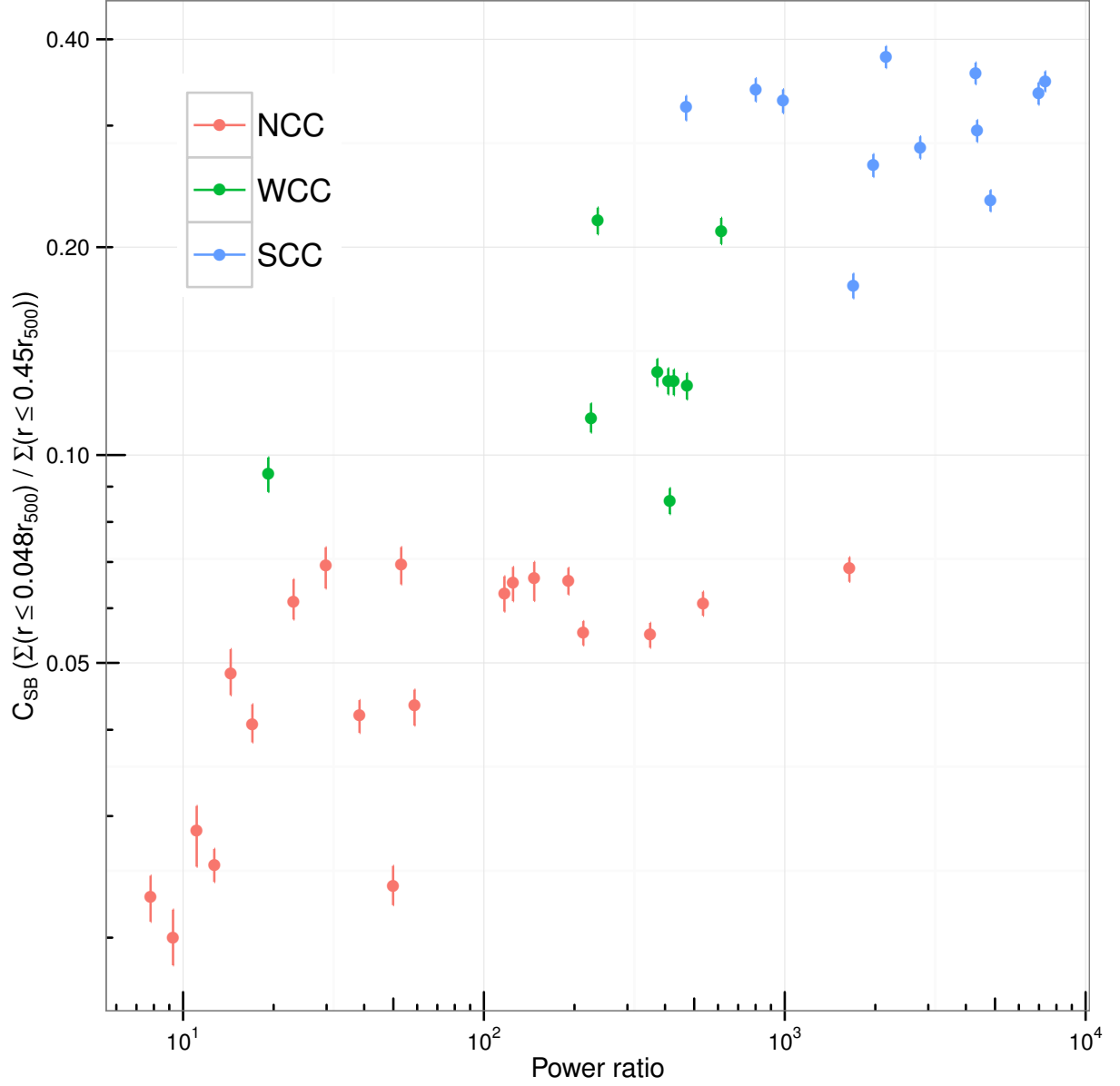


Fig. 3.— The relative core brightness against the power ratio, see §3.2.5. The power ratio is defined as the ratio of power at $0.35r_{500}$ to that at large wavenumbers where image power spectra reduce to a constant component. The SCC-WCC-NCC classifications depend on three traditional diagnostics, see §3.2.4

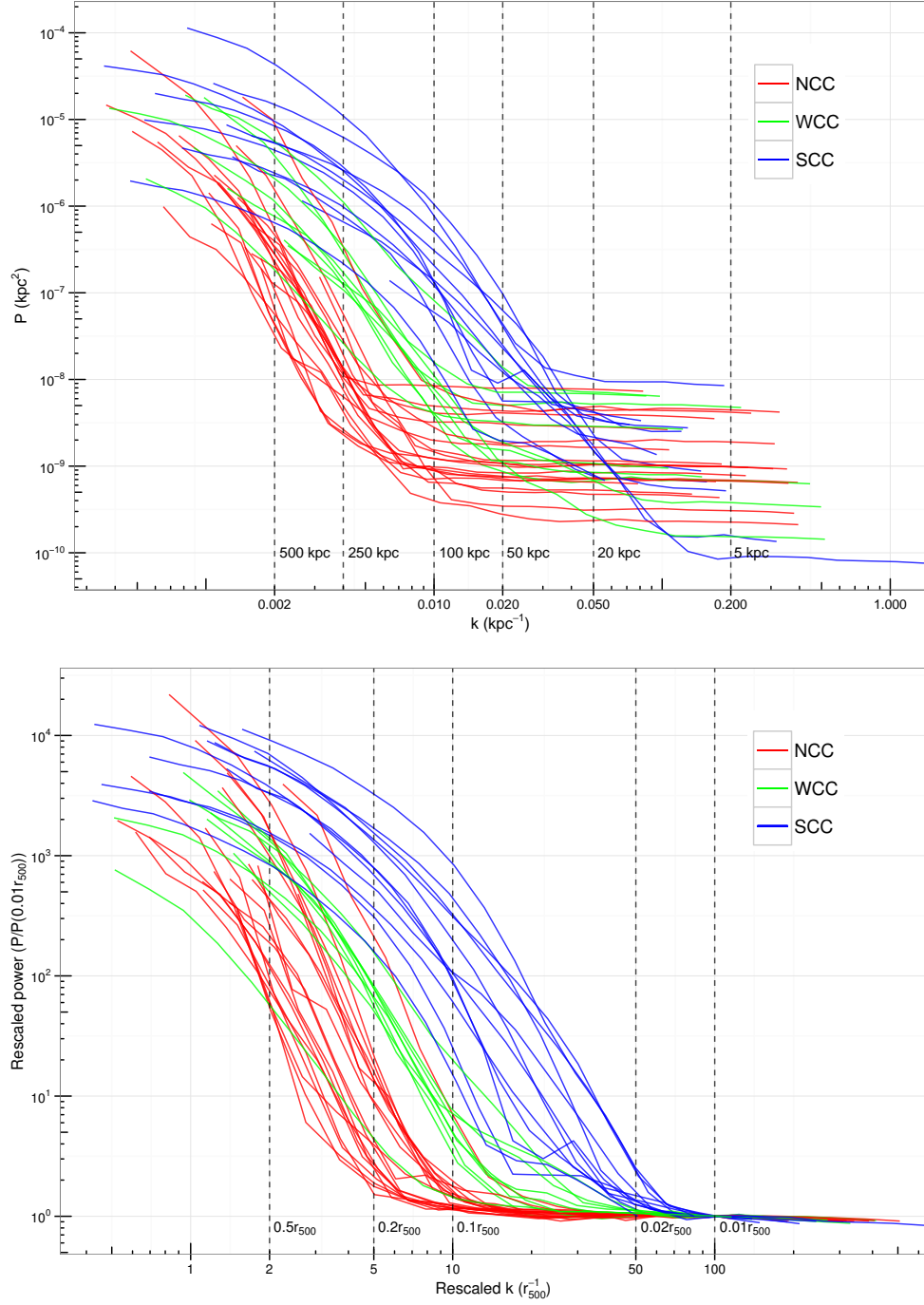


Fig. 4.— *Top* : Observed two-dimensional power spectra of all sample clusters. *Bottom* : The same as top but scaled by r_{500} and the power at $0.01r_{500}$, and the typical error are about 10% for small wavenumbers and 20% for large wavenumbers .

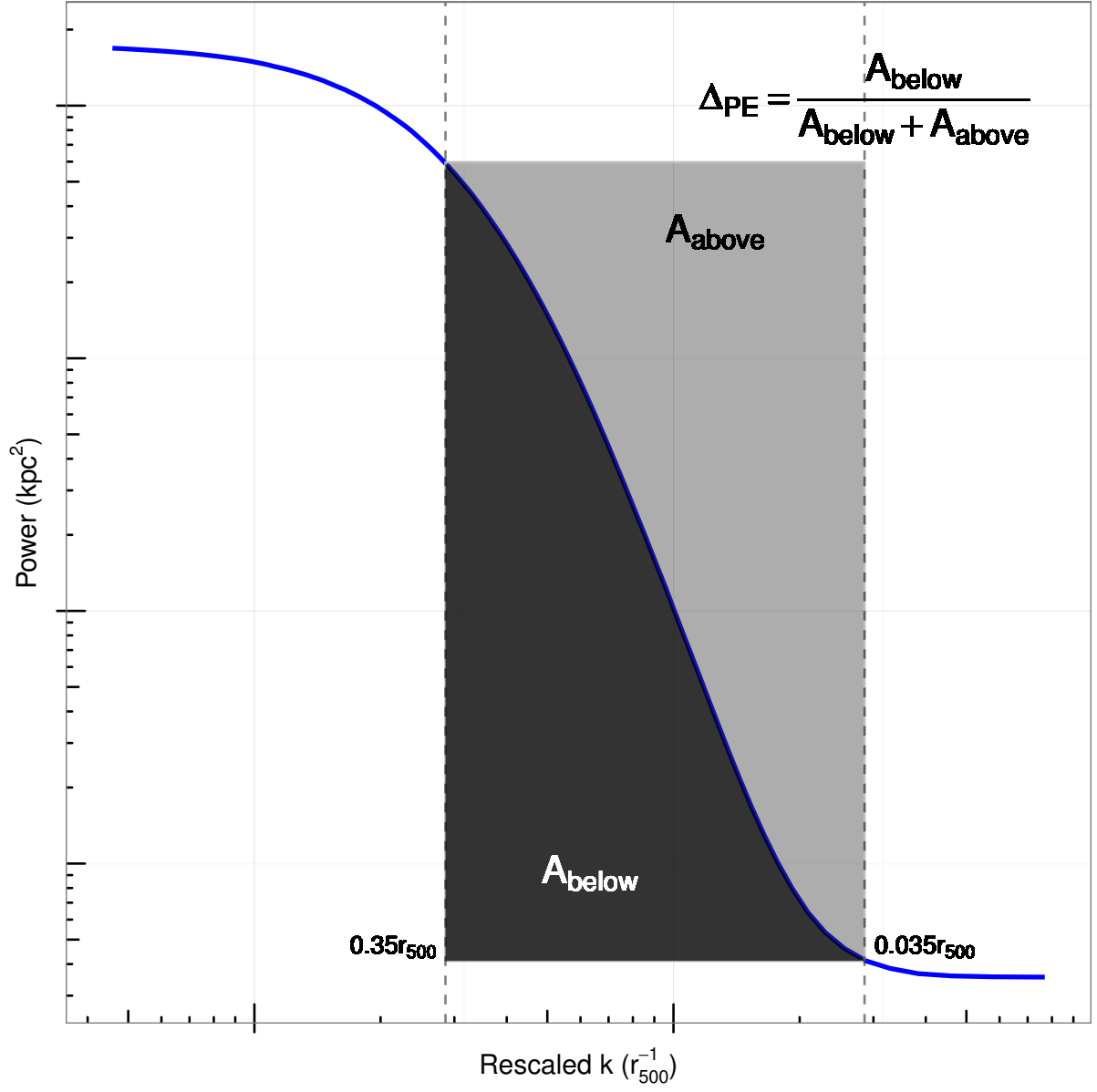


Fig. 5.— Definition of power excess index (PEI).

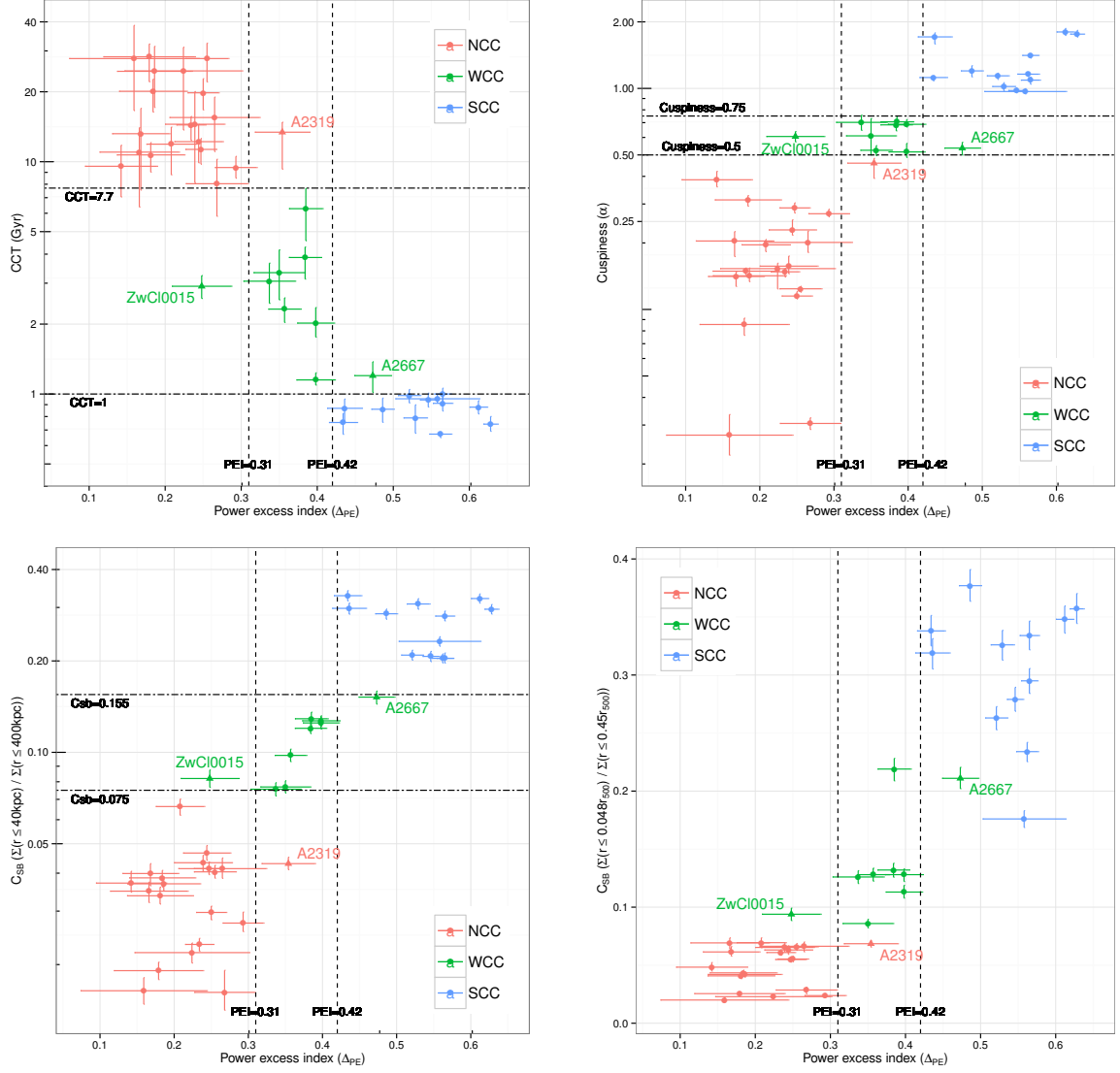


Fig. 6.— A comparison between the SCC-WCC-NCC classifications derived with the PEI diagnostic and three traditional diagnostics. The relation between the relative core brightness (§3.2.5) and PEI is also plotted (lower right).

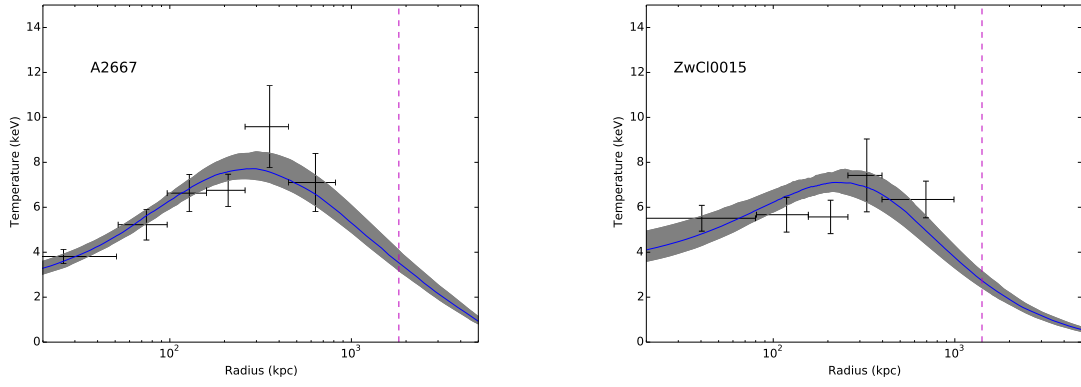


Fig. 7.— Gas temperature profiles of A2667 and ZwCl0015 obtained with *Chandra*, and the red dotted line presents the $1.5r_{500}$.

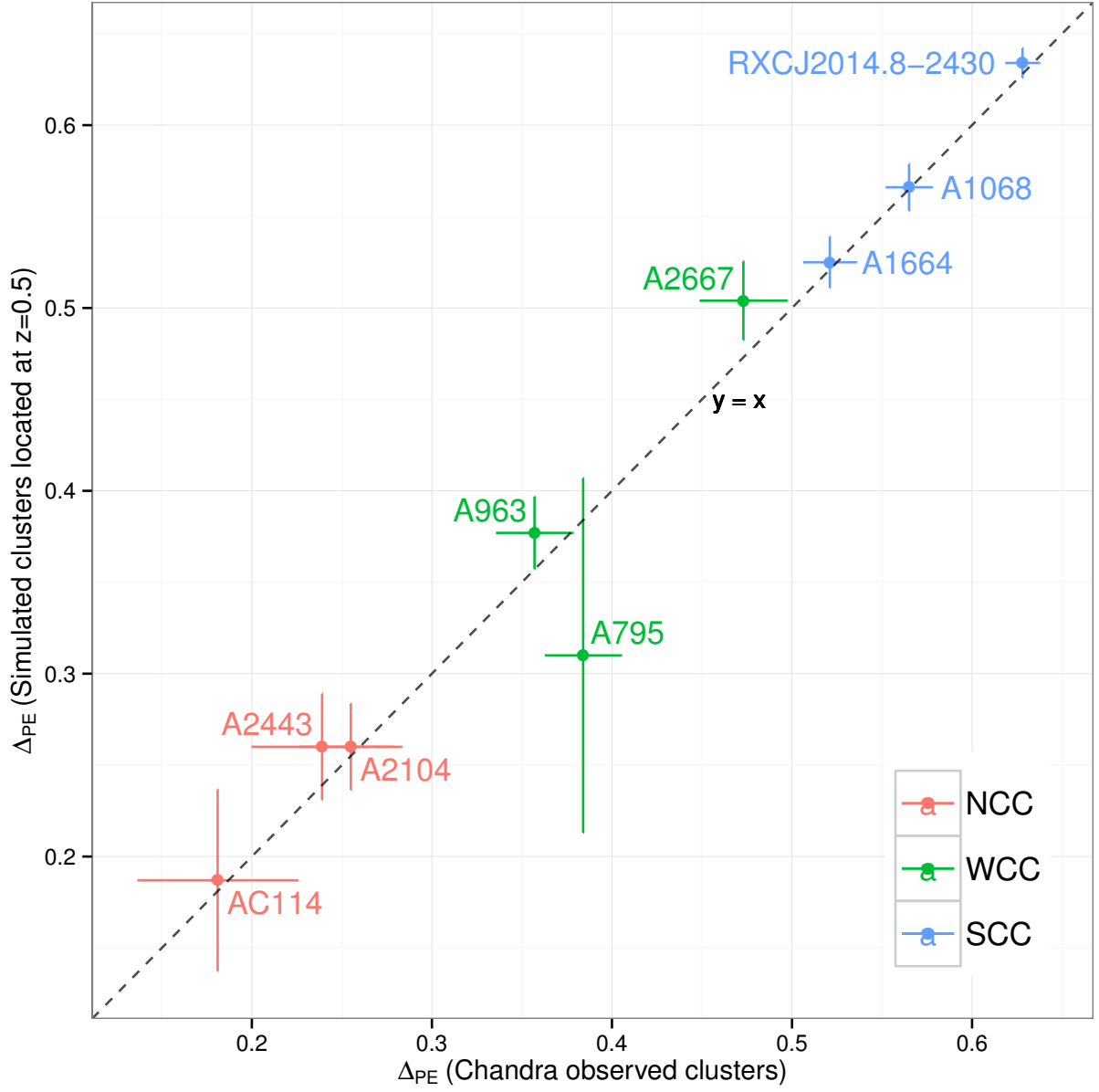


Fig. 8.— A comparison between PEI classifications based on the observed Chandra data and the data simulated for $z=0.5$.

REFERENCES

- Arnaud, K. A. 1996, *Astronomical Data Analysis Software and Systems V*, 101, 17
- Ashman, K. M., Bird, C. M., & Zepf, S. E. 1994, *AJ*, 108, 2348
- Baldi, A., Forman, W., Jones, C., et al. 2009, *ApJ*, 707, 1034
- Bauer, F. E., Fabian, A. C., Sanders, J. S., Allen, S. W., & Johnstone, R. M. 2005, *MNRAS*, 359, 1481
- Best, P. N., von der Linden, A., Kauffmann, G., Heckman, T. M., & Kaiser, C. R. 2007, *MNRAS*, 379, 894
- Blanton, E. L., Randall, S. W., Clarke, T. E., et al. 2011, *ApJ*, 737, 99
- Bouwens, R., Broadhurst, T., & Silk, J. 1998, *ApJ*, 506, 557
- Burns, J. O. 1990, *AJ*, 99, 14
- Burns, J. O., Hallman, E. J., Gantner, B., Motl, P. M., & Norman, M. L. 2008, *ApJ*, 675, 1125
- Carter, J. A., & Read, A. M. 2007, *A&A*, 464, 1155
- Cavaliere, A., & Fusco-Femiano, R. 1976, *A&A*, 49, 137
- Chen, Y., Reiprich, T. H., Böhringer, H., Ikebe, Y., & Zhang, Y.-Y. 2007, *A&A*, 466, 805
- Churazov, E., Vikhlinin, A., Zhuravleva, I., et al. 2012, *MNRAS*, 421, 1123
- Donahue, M., Voit, G. M., O’Dea, C. P., Baum, S. A., & Sparks, W. B. 2005, *ApJ*, 630, L13
- Dickey, J. M., & Lockman, F. J. 1990, *ARA&A*, 28, 215
- Donahue, M. 2007, *Heating versus Cooling in Galaxies and Clusters of Galaxies*, 20

- Dunn, R. J. H., & Fabian, A. C. 2006, MNRAS, 373, 959
- Eilek, J. A. 2004, The Riddle of Cooling Flows in Galaxies and Clusters of galaxies, 165
- Fabian, A. C. 1994, ARA&A, 32, 277
- Fabian, A. C., Sanders, J. S., Taylor, G. B., et al. 2006, MNRAS, 366, 417
- Fabian, A. C. 2012, ARA&A, 50, 455
- Feretti, L., Giovannini, G., Govoni, F., & Murgia, M. 2012, A&A Rev., 20, 54
- Freeman, P. E., Kashyap, V., Rosner, R., & Lamb, D. Q. 2002, ApJS, 138, 185
- Gastaldello, F., Buote, D. A., Brighenti, F., & Mathews, W. G. 2008, ApJ, 673, L17
- Grevesse, N., & Sauval, A. J. 1998, Space Sci. Rev., 85, 161
- Gu, L., Xu, H., Gu, J., et al. 2012, ApJ, 749, 186
- Hudson, D. S., Mittal, R., Reiprich, T. H., et al. 2010, A&A, 513, A37
- Humphrey, P. J., & Buote, D. A. 2006, ApJ, 639, 136
- Jones, C., & Forman, W. 1984, ApJ, 276, 38
- Kalberla, P. M. W., Burton, W. B., Hartmann, D., et al. 2005, A&A, 440, 775
- Kushino, A., Ishisaki, Y., Morita, U., et al. 2002, PASJ, 54, 327
- Makishima, K., Ezawa, H., Fukuzawa, Y., et al. 2001, PASJ, 53, 401
- McLachlan, G. J., & Basford, K. E. 1988, Statistics: Textbooks and Monographs, New York: Dekker, 1988
- McNamara, B. R., & Nulsen, P. E. J. 2007, ARA&A, 45, 117

- Mittal, R., Hudson, D. S., Reiprich, T. H., & Clarke, T. 2009, *A&A*, 501, 835
- Molendi, S., & Pizzolato, F. 2001, *ApJ*, 560, 194
- Mushotzky, R. F., Cowie, L. L., Barger, A. J., & Arnaud, K. A. 2000, *Nature*, 404, 459
- Navarro, J. F., Frenk, C. S., & White, S. D. M. 1996, *ApJ*, 462, 563
- O’Hara, T. B., Mohr, J. J., & Guerrero, M. A. 2004, *ApJ*, 604, 604
- O’Hara, T. B., Mohr, J. J., Bialek, J. J., & Evrard, A. E. 2006, *ApJ*, 639, 64
- O’Sullivan, E., Giacintucci, S., David, L. P., Vrtillek, J. M., & Raychaudhury, S. 2010, *MNRAS*, 407, 321
- Peres, C. B., Fabian, A. C., Edge, A. C., et al. 1998, *MNRAS*, 298, 416
- Rafferty, D. A., McNamara, B. R., Nulsen, P. E. J., & Wise, M. W. 2006, *ApJ*, 652, 216
- Rebusco, P., Churazov, E., Böhringer, H., & Forman, W. 2005, *MNRAS*, 359, 1041
- Rebusco, P., Churazov, E., Böhringer, H., & Forman, W. 2006, *MNRAS*, 372, 1840
- Reiprich, T. H. 2001, Ph.D. Thesis
- Reiprich, T. H., & Böhringer, H. 2002, *ApJ*, 567, 716
- Rizza, E., Burns, J. O., Ledlow, M. J., et al. 1998, *MNRAS*, 301, 328
- Sanderson, A. J. R., Ponman, T. J., & O’Sullivan, E. 2006, *MNRAS*, 372, 1496
- Santos, J. S., Rosati, P., Tozzi, P., et al. 2008, *A&A*, 483, 35
- Smith, R. K., Brickhouse, N. S., Liedahl, D. A., & Raymond, J. C. 2001, *ApJ*, 556, L91
- Storm, E., Jeltama, T. E., & Rudnick, L. 2015, *MNRAS*, 448, 2495

Sun, M., Voit, G. M., Donahue, M., et al. 2009, *ApJ*, 693, 1142

Sun, M. 2009, *ApJ*, 704, 1586

Vikhlinin, A., Burenin, R., Forman, W. R., et al. 2007, *Heating versus Cooling in Galaxies and Clusters of Galaxies*, 48

Walker, S. A., Sanders, J. S., & Fabian, A. C. 2015, *MNRAS*, 453, 3699

White, D. A., Jones, C., & Forman, W. 1997, *MNRAS*, 292, 419

Wise, M. W., McNamara, B. R., Nulsen, P. E. J., Houck, J. C., & David, L. P. 2007, *ApJ*, 659, 1153

Zhao, H.-H., Li, C.-K., Chen, Y., Jia, S.-M., & Song, L.-M. 2015, *ApJ*, 799, 47

Zhuravleva, I., Churazov, E., Arévalo, P., et al. 2015, *MNRAS*, 450, 4184